The Astrophysical Journal Letters, 913:L24 (7pp), 2021 June 1 https://doi.org/10.3847/2041-8213/abfcc7

Giant Metrewave Radio Telescope Detection of HI 21 cm Emission from Star-forming Galaxies at $z \approx 1.3$

Aditya Chowdhury[1], Nissim Kanekar[1], Barnali Das[1], K. S. Dwarakanath[2], and Shiv Sethi[2]
[1] National Centre for Radio Astrophysics, Tata Institute of Fundamental Research, Pune, India; chowdhury@ncra.tifr.res.in
[2] Department of Astronomy and Astrophysics, Raman Research Institute, Bangalore, India
Received 2021 April 9; revised 2021 April 28; accepted 2021 April 28; published 2021 May 31

Abstract

We report a ≈400 hr Giant Metrewave Radio Telescope (GMRT) search for HI 21 cm emission from star-forming galaxies at $z = 1.18$–1.39 in seven fields of the DEEP2 Galaxy Survey. Including data from an earlier 60 hr GMRT observing run, we co-added the HI 21 cm emission signals from 2841 blue star-forming galaxies that lie within the FWHM of the GMRT primary beam. This yielded a 5.0σ detection of the average HI 21 cm signal from the 2841 galaxies at an average redshift $\langle z \rangle \approx 1.3$, only the second detection of HI 21 cm emission at $z \geqslant 1$. We obtain an average HI mass of $\langle M_{HI} \rangle = (3.09 \pm 0.61) \times 10^{10}\, M_\odot$ and an HI-to-stellar mass ratio of 2.6 ± 0.5, both significantly higher than values in galaxies with similar stellar masses in the local universe. We also stacked the 1.4 GHz continuum emission of the galaxies to obtain a median star formation rate (SFR) of $14.5 \pm 1.1\ M_\odot yr^{-1}$. This implies an average HI depletion timescale of ≈2 Gyr for blue star-forming galaxies at $z \approx 1.3$, a factor of ≈3.5 lower than that of similar local galaxies. Our results suggest that the HI content of galaxies toward the end of the epoch of peak cosmic SFR density is insufficient to sustain their high SFR for more than ≈2 Gyr. Insufficient gas accretion to replenish the HI could then explain the observed decline in the cosmic SFR density at $z < 1$.

Unified Astronomy Thesaurus concepts: Radio spectroscopy (1359); Neutral hydrogen clouds (1099); Galaxy evolution (594)

1. Introduction

Understanding galaxy evolution requires us to understand the evolution of, and the interplay between, the two main baryonic components of galaxies, the stars and the interstellar medium (ISM). For most galaxies in the local universe, the dominant component of the ISM, by mass, is neutral atomic hydrogen (HI), the primary fuel for star formation. The HI mass of different types of galaxies, and the relations between the HI mass and the molecular gas mass, the stellar mass, and the star formation rate (SFR), are thus critical inputs to studies of galaxy evolution. In the local universe, the HI mass of galaxies has long been measured via emission studies in the HI 21 cm emission line. Unfortunately, the low Einstein A-coefficient of this transition has meant that it has not been possible to detect HI 21 cm emission from individual galaxies beyond even fairly low redshifts, $z \gtrsim 0.4$, with the highest-redshift detection to date at $z = 0.376$ (e.g., Fernández et al. 2016).

Over the past two decades, the contrast between the dramatic improvement in measurements of the stellar properties of high-z galaxies (e.g., Madau & Dickinson 2014) and the lack of information on their HI properties has become more and more stark. For example, it is now well known that the SFR density of the universe increases steadily from $z \approx 8$ to $z \approx 3$–4, remains flat from $z \approx 3$ to $z \approx 1$, and then declines precipitously, by an order of magnitude, from $z \approx 1$ to the present epoch (e.g., Le Floc'h et al. 2005; Hopkins & Beacom 2006; Bouwens et al. 2010). The causes of this evolution, especially the steep decline in the SFR density after $z \approx 1$, remain unclear today. Measurements of the fuel for star formation, the HI content of galaxies, especially during the peak epoch of star formation in the universe, $z \approx 1$–3, are critical to understanding the evolution of the SFR density.

While measurements of the HI masses of individual galaxies at $z \approx 1$ would require prohibitively large integrations with today's radio telescopes, progress can be made by "stacking" the HI 21 cm emission signals of a large number of galaxies with known spectroscopic redshifts that lie within the primary beam of a radio interferometer (Zwaan 2000; Chengalur et al. 2001). Such HI 21 cm stacking yields a measurement of the *average* HI content of the stacked galaxies, and thus allows one to obtain statistical information about the HI properties of different galaxy populations at the redshift of interest. Until recently, even such HI 21 cm stacking studies were mostly limited by sensitivity and frequency coverage to relatively low redshifts, $z \lesssim 0.4$ (e.g., Lah et al. 2007; Rhee et al. 2016; Bera et al. 2019), with a single search at $z > 1$ yielding a nondetection of the stacked HI 21 cm emission signal and an upper limit to the average HI mass of a sample of star-forming galaxies at $z \approx 1.3$ (Kanekar et al. 2016).

Recently, Chowdhury et al. (2020) used the new 550–850 MHz receivers and the new wideband correlator of the upgraded Giant Metrewave Radio Telescope (GMRT) to obtain the first detection of the stacked HI 21 cm emission signal at $z \approx 1$. They stacked the HI 21 cm emission signals from 7653 star-forming galaxies at $z = 0.74$–1.45 in the DEEP2 Galaxy Survey fields (Newman et al. 2013), to measure the average HI mass of star-forming galaxies at $z \approx 1$. In this Letter, we report an independent ≈400 hr GMRT search for HI 21 cm emission from a sample of star-forming galaxies at $z \approx 1.18$–1.39, also in the DEEP2 Survey fields, carried out using the original GMRT 610 MHz receivers and the legacy narrowband GMRT correlator.

2. Observations and Data Analysis

The HI 21 cm stacking technique requires a large number of galaxies with accurate spectroscopic redshifts (velocity error, $\Delta V \lesssim 100\ km\ s^{-1}$; e.g., Maddox et al. 2013) within the primary beam of the interferometer, and with redshifts such that the HI

Table 1
Details of the Observations

Field	R.A. (J2000)	Decl. (J2000)	On-source Time (hr)		$\sigma_{\rm cont}$	Beam	Number of Galaxies		$\sigma_{\rm HI}$	
			A	B	μJy/beam	(Continuum)	A	B	μJy/beam	
									A	B
21	$16^{\rm h}47^{\rm m}54^{\rm s}.00$	$34°56'00''.0$	24.6	23.9	12	$4''.5 \times 3''.8$	103	122	239	184
22	$16^{\rm h}50^{\rm m}54^{\rm s}.00$	$34°56'00''.0$	16.8	16.4	17	$4''.4 \times 3''.8$	147	142	296	342
31	$23^{\rm h}27^{\rm m}00^{\rm s}.00$	$00°07'00''.0$	18.5	13.6	12	$5''.4 \times 4''.0$	148	154	250	280
32	$23^{\rm h}29^{\rm m}30^{\rm s}.00$	$00°10'00''.0$	21.9	19.5	11	$5''.3 \times 4''.0$	183	128	228	210
33	$23^{\rm h}33^{\rm m}00^{\rm s}.00$	$00°07'00''.0$	15.0	19.5	13	$5''.5 \times 3''.9$	159	136	271	175
41	$02^{\rm h}27^{\rm m}30^{\rm s}.00$	$00°35'00''.0$	15.7	17.1	15	$5''.3 \times 3''.9$	188	204	288	316
42	$02^{\rm h}30^{\rm m}00^{\rm s}.00$	$00°35'00''.0$	19.7	20.3	14	$5''.5 \times 3''.8$	92	262	213	265
21	$16^{\rm h}47^{\rm m}54^{\rm s}.00$	$34°56'00''.0$	8.5 (C)		16[a]	$6''.7 \times 5''.2$	146		323	
22	$16^{\rm h}50^{\rm m}54^{\rm s}.00$	$34°56'00''.0$	8.5 (C)		18[a]	$5''.2 \times 4''.3$	154		259	
31/32	$23^{\rm h}28^{\rm m}00^{\rm s}.00$	$00°09'00''.0$	13.0 (D)		17[a]	$5''.9 \times 4''.6$	185		309	
32/33	$23^{\rm h}32^{\rm m}00^{\rm s}.00$	$00°09'00''.0$	13.0 (D)		13[a]	$6''.1 \times 4''.4$	188		289	

Note. The first seven rows describe the ≈400 hr GMRT observations presented in this Letter, while the last four rows are for the data of Kanekar et al. (2016). The columns are (1) the DEEP2 subfield targeted by the GMRT pointing, (2)–(3) the J2000 coordinates of the pointing center, (4) the on-source time for each frequency setting, where setting A covers 591.0–624.3 MHz, setting B covers 616.0–649.3 MHz, setting C covers 601.0–634.3 MHz, and setting D covers 626.0–659.3 MHz (note that a single frequency setting was used for each pointing by Kanekar et al. 2016), (5) the rms noise on the continuum image, in μJy/beam, (6) the synthesized beam of the continuum image, (7) the final number of galaxies used for the stacking analysis from each frequency setting and each GMRT pointing, (8) the median rms noise per 34 km s^{-1} channel on the HI 21 cm spectra of the final sample of galaxies in each frequency setting and GMRT pointing, after correcting for their location in the GMRT primary beam

[a] The continuum images are from Bera et al. (2018).

21 cm line is redshifted into the frequency band of the telescope. The DEEP2 galaxy redshift survey (Newman et al. 2013) provides spectroscopic redshifts with $\Delta V \lesssim 55$ km s^{-1} for galaxies at $z \approx 0.7$–1.5, in fields that can be optimally covered by the GMRT primary beam at ≈610 MHz (e.g., Kanekar et al. 2016; Chowdhury et al. 2020). This made the DEEP2 fields the ideal targets for our GMRT HI 21 cm emission survey at $z \approx 1.3$. We used one GMRT pointing to cover each of the seven DEEP2 subfields 21, 22, 31, 32, 33, 41, and 42 (Newman et al. 2013).

We observed the DEEP2 fields with the original GMRT 610 MHz receivers for a total of ≈400 hr between 2015 May and 2016 November (project codes: 28_097, 29_034, 30_069, 31_118; PI: N. Kanekar). We used the GMRT Software Backend (GSB) as the correlator, with a 33.3 MHz observing band, sub-divided into 512 spectral channels. For each pointing, we used two frequency settings, 591.0–624.3 MHz and 616.0–649.3 MHz, to cover the HI 21 cm line from the redshift range $z = 1.19$–1.39, with a velocity resolution of ≈30–33 km s^{-1}. We carried out seven pointings on the DEEP2 fields, with a total time of ≈40–60 hr per pointing, split approximately evenly between the two frequency settings. Observations of one or more of 3C286, 3C48 and 3C147 in each observing run were used to calibrate the flux density scale, while observations of the compact sources $0022+002$, $0204+152$, or $1609+266$ were used to calibrate the complex antenna gains and bandpass shapes. The total on-source time for each pointing, combining the two frequency settings, was ≈32–49 hr. The observational details are summarized in Table 1.

All data were analyzed in the Common Astronomy Software Applications Package (CASA version 5; McMullin et al. 2007), following standard procedures. The AOFLAGGER package (Offringa et al. 2012) was additionally used for excision of data affected by radio frequency interference (RFI). For each pointing, after initial excision of non-working antennas and data affected by RFI, and calibration of the antenna gains and bandpasses, the target visibilities of the two frequency settings were combined, and a standard self-calibration procedure carried out on the combined data set. The antenna-based complex gains and bandpasses at all stages of the analysis were determined using a custom package within the CASA framework; the complex gain solver in this package is robust to the presence of outliers in the data.[3] We note that, at the time when the data were being analyzed, the CASA calibration routines did not contain robust solvers, and were hence unstable in the presence of RFI, typical at these low radio frequencies. Imaging was done using the CASA task TCLEAN, with w-projection (Cornwell et al. 2008), and MT-MFS (first-order expansion; Rau & Cornwell 2011); we used Briggs weighting with a robust parameter of −0.5 (Briggs 1995) during self-calibration and a robust parameter of 0.0 for the final continuum imaging. For each target field, a region of size $\approx 1.^{\circ}8 \times 1.^{\circ}8$ was imaged, extending far beyond the null of the GMRT primary beam at these frequencies. The final continuum images obtained after self-calibration are shown in Figure 1; the images have an rms noise of ≈11–17μJy/beam, away from radio-continuum sources, with a synthesized beam of ≈3.″8–5.″5 (see Table 1).

Next, the continuum emission of each field was subtracted from the self-calibrated visibilities using the tasks UVSUB, followed by MSTRANSFORM; the latter task was also used to regrid the visibilities to the barycentric velocity frame. Following this, the continuum-subtracted and regridded visibilities of each pointing and frequency setting were used to make the final spectral cubes; this was done using w-projection and Briggs weighting with a robust parameter of +1 (Briggs 1995). We experimented with different choices of the robust parameter, and found that a robust parameter of

[3] The package is publicly available at https://github.com/chowdhuryaditya/calR and is archived in Zenodo (Chowdhury 2021).

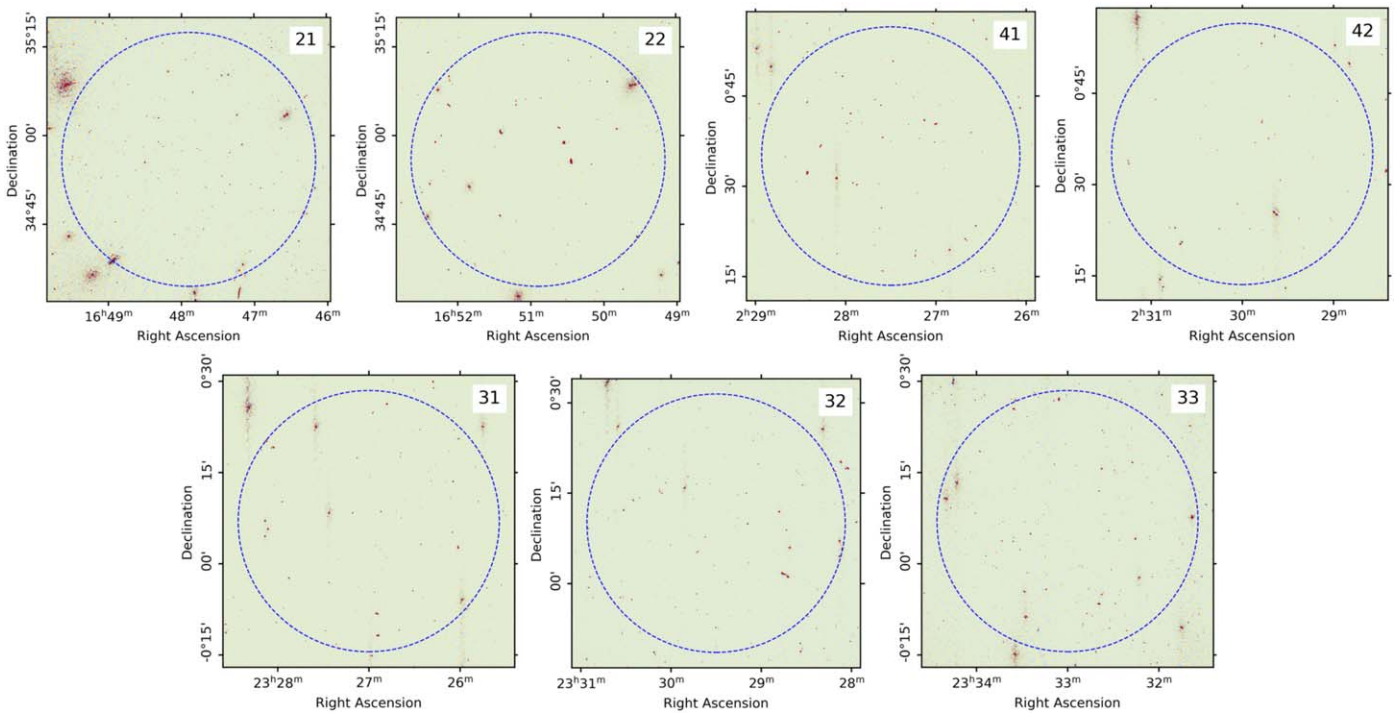

Figure 1. The GMRT 610 MHz continuum images of the seven DEEP2 subfields from the ≈400 hr of data presented here. The blue dotted circle in each panel marks the FWHM of the GMRT primary beam at 610 MHz.

+1 suppresses the spatial extent of deconvolution errors around bright radio-continuum sources while having a negligible effect on the rms noise of the cube. The final spectral cubes have an angular resolution of ≈5.″3–8.″0, corresponding to spatial resolutions of ≈46 kpc–67 kpc at $z \approx 1.3$.[4]

Besides the ≈400 hr of new GMRT data, we also made new spectral cubes (again with w-projection and a robust parameter of +1) from the self-calibrated and continuum-subtracted visibilities of the 60 hr data set of Kanekar et al. (2016). These observations also used the GMRT 610 MHz receivers and the GSB as the correlator, with a 33.3 MHz bandwidth and 512 channels. Four GMRT pointings were observed, each with a single frequency setting, covering 601.0–634.3 MHz or 626.0–659.3 MHz. For completeness, we present a summary of these observations in Table 1.

We corrected for any offset in the astrometry of our images using our recent upgraded GMRT images of these fields (e.g., Chowdhury et al. 2020); the astrometry of the latter images has been verified to be consistent with that of the DEEP2 survey (Newman et al. 2013). In all cases, the positional offset of the images was comparable to or lower than the FWHM of the synthesized beam of the final continuum image.

3. Stacking the HI 21 cm Emission Signals

The DEEP2 DR4 catalog contains 3109 galaxies with accurate redshifts (Redshift Quality Code, $Q \geqslant 3$; Newman et al. 2013), for which the redshifted HI 21 cm line frequency lies within our frequency coverage, and that lie within the FWHM of the GMRT primary beam at the redshifted HI 21 cm line frequency. However, the HI 21 cm lines of some of these 3109 galaxies were covered multiple times, due to their location in the overlap region of the seven new GMRT pointings, or due to the galaxies being covered in the GMRT pointings of both the ≈400 hr new data set and the observations of Kanekar et al. (2016). Accounting for the multiple observations, we have a total of 3996 independent HI 21 cm spectra; for simplicity, we will hereafter refer to each of these spectra as arising from individual galaxies (i.e., will ignore the fact that some of the spectra are from the same object). Of the 3996 "galaxies," 3142 are covered by the ≈400 hr of new data, while 854 galaxies are from Kanekar et al. (2016).

We imposed further restrictions on the above sample of 3996 galaxies to ensure homogeneity of the sample and good data quality. The selection criteria as well as the procedure to stack the HI 21 cm emission of the final sample are similar to those used by Chowdhury et al. (2020). First, the DEEP2 selection criterion ($R \leqslant 24.1$; Newman et al. 2013) preferentially picks out blue star-forming galaxies at $z \gtrsim 1$ (e.g., Weiner et al. 2009). To ensure homogeneity in our sample, we excluded the 162 galaxies that are part of the "red cloud" in the color–magnitude diagram (Willmer et al. 2006). We further excluded 238 radio-loud AGNs from our sample, in order to restrict ourselves to star-forming galaxies; the AGNs were identified based on their detection at $\geqslant 4\sigma$ significance in our continuum images, with a rest-frame 1.4 GHz luminosity $>2 \times 10^{23}$ W Hz^{-1} (Condon et al. 2002).[5] After excluding red galaxies and AGNs, our sample contains 3596 blue star-forming galaxies, at $z = 1.18$–1.39.

We next extracted three-dimensional subcubes around each of the 3596 galaxies, and convolved the subcubes to a uniform beam of 60 kpc at the redshift of each galaxy. At this stage, we excised any spectral channels whose intrinsic synthesized beam

[4] Throughout this work, we use a flat Λ cold dark matter (ΛCDM) cosmology, with (H_0, Ω_m, Ω_Λ) = (70 km s^{-1} Mpc^{-1}, 0.3, 0.7).

[5] We note that in our earlier papers (e.g., Bera et al. 2019; Chowdhury et al. 2020), the same quantity was referred to as "luminosity density"; here we use "luminosity" throughout, to be consistent with the usage in radio astronomy.

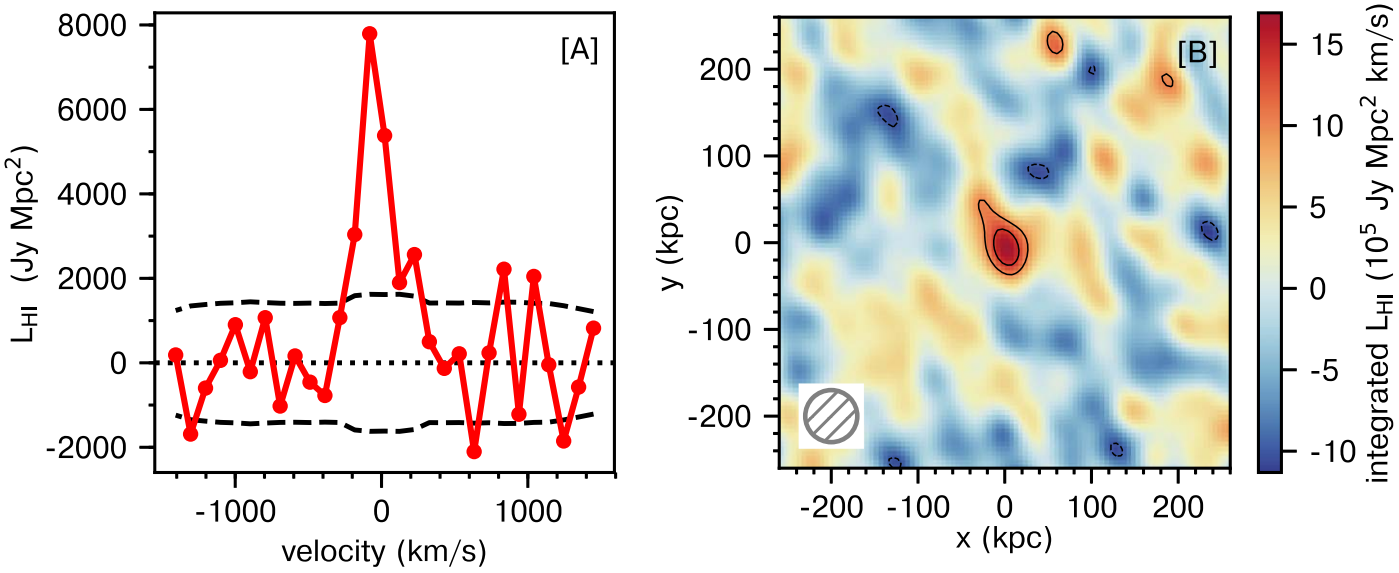

Figure 2. (A) The average HI 21 cm spectrum, at a velocity resolution of 102 km s^{-1}, obtained after stacking the individual HI 21 cm spectra at the location of the 2841 blue star-forming galaxies at $z = 1.18$–1.39. The dashed lines show the 1σ uncertainty on the spectrum. A clear detection of the average HI 21 cm signal can be seen in the central velocity channels. (B) The average HI 21 cm emission image obtained by combining the central channels of the stacked cube. The circle at the bottom left indicates the 60 kpc resolution of the image. The contours are at $(-3, 3, 4.2) \times \sigma$ levels, with dashed negative contours. A clear detection of the average HI 21 cm emission is obtained at the center of the image.

is >60 kpc. We then regridded each convolved subcube to the same spatial and spectral grid, with spatial pixels of size 5.2 kpc, covering ±260 kpc around each galaxy, and velocity channels of 34 km s^{-1}, covering ±1500 km s^{-1} around the galaxy's redshifted HI 21 cm line frequency. We then fitted a second-order spectral baseline to each spatial pixel of all subcubes, and subtracted out this baseline; this removes systematic effects caused by deconvolution errors and bandpass inaccuracies.

Next, we inspected the HI 21 cm spectra at the locations of the 3596 galaxies for any systematic effects that might limit the rms noise on the final stacked HI 21 cm spectrum. This was done by testing the spectra for Gaussianity, following the approach of Chowdhury et al. (2020). The *p*-value thresholds chosen for the Gaussianity tests are slightly different from those in Chowdhury et al. (2020); however, the exact *p*-value thresholds do not have a significant impact on our results. After excluding 755 galaxies that fail the Gaussianity tests, our sample contains 2841 blue star-forming galaxies at $z = 1.18$–1.39, of which 2168 galaxies are from the new data presented here, with the remaining 673 galaxies from the data set of Kanekar et al. (2016). The last four columns of Table 1 list, for each pointing and frequency setting, the number of galaxies and the median rms noise per 34 km s^{-1} channel on the HI 21 cm spectra.

For each subcube, we converted the HI 21 cm flux density (S_{HI}) to the HI 21 cm line luminosity (L_{HI}), using the relation $L_{HI} = 4\pi\ S_{HI}\ {D_L}^2/(1+z)$, where D_L is the luminosity distance of the galaxy. We then stacked, pixel by pixel, the three-dimensional HI 21 cm subcubes of each of the 2841 galaxies. While stacking, we weighted each galaxy by the inverse of the rms noise on its HI 21 cm spectrum, in luminosity units. Finally, we fitted a second-order spectral baseline to each pixel of the stacked cube, excluding the central ±250 km s^{-1}, and subtracted out this baseline.

We estimated the rms noise on the final stacked HI 21 cm cube via a Monte Carlo simulation, where we randomly shifted the velocity of the individual galaxies within ±1500 km s^{-1}, and then stacked the velocity-shifted subcubes, to obtain a realization of a stacked noise cube. We performed 10,000 realizations of this simulation to determine the rms noise on the final stacked HI 21 cm cube.

The final stacked HI 21 cm spectrum, obtained by taking a cut through the center of the stacked cube (i.e., at the position of the stacked galaxies), is shown, at a velocity resolution of 102 km s^{-1}, in Figure 2(A). The dotted line in the figure shows the $\pm1\sigma$ uncertainty derived from the Monte Carlo simulation described above. We obtain a clear detection, with 5.0σ statistical significance, of the average HI 21 cm emission signal from the 2841 galaxies at an average redshift of $\langle z \rangle \approx 1.3$. Figure 2(B) shows the velocity-integrated HI 21 cm emission image, obtained by adding the central three velocity channels of the final stacked HI 21 cm cube. The image also shows a clear detection of the HI 21 cm emission signal in the central region. Integrating over the stacked HI 21 cm line profile yields a velocity-integrated HI 21 cm line luminosity of $(16.5 \pm 3.3) \times 10^5$ Jy Mpc^2 km s^{-1}. This corresponds to an average HI mass of $\langle M_{HI} \rangle = (3.09 \pm 0.61) \times 10^{10}\ M_\odot$, for the 2841 blue star-forming galaxies at $\langle z \rangle \approx 1.3$.

We tested whether the HI 21 cm emission is extended on scales larger than 60 kpc by carrying out the stacking procedure after smoothing to coarser spatial resolutions. We find that increasing the size of the beam beyond 60 kpc does not result in a statistically significant increase in the average HI 21 cm emission signal. We thus find no evidence that the average HI 21 cm emission from star-forming galaxies at $\langle z \rangle \approx 1.3$ arises from a region larger than 60 kpc.

The narrow beam of our GMRT observations implies that the effect of "source confusion" on our results is negligible. For example, Chowdhury et al. (2020) estimated that the HI 21 cm emission from companion galaxies is very unlikely to lie within both the 60 kpc beam and within ≈±200 km s^{-1} of the target galaxies. They found that companion galaxies contribute $\lesssim$2% to the stacked HI 21 cm emission signal.

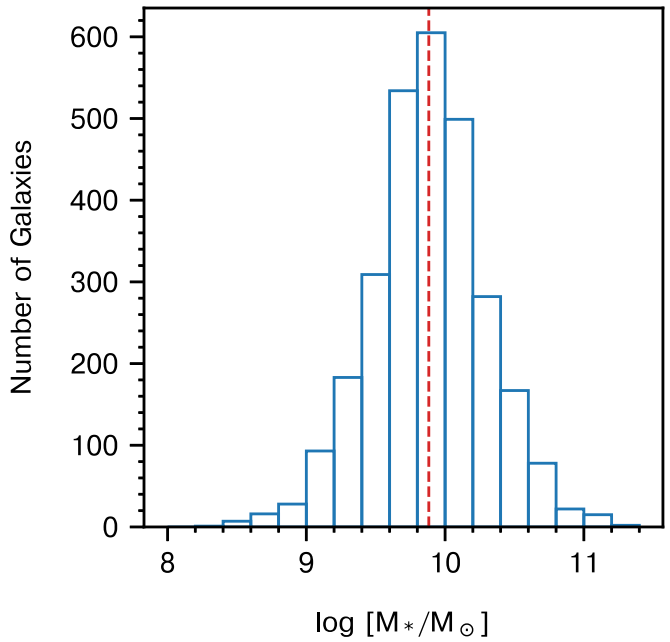

Figure 3. The stellar mass distribution of our sample of 2841 blue star-forming galaxies at $z \approx 1.3$. The dashed red vertical line shows the median stellar mass of the sample.

The 2841 blue star-forming galaxies at $z \approx 1.3$ have stellar masses in the range $M_* \approx 10^8$–$10^{11.5}\,M_\odot$, with a mean stellar mass of $\langle M_* \rangle = 1.2 \times 10^{10}\,M_\odot$.[6] Figure 3 shows the distribution of stellar masses of our sample galaxies. We split the 2841 galaxies into two subsamples, with stellar masses above and below their median stellar mass of $M_* = 7.6 \times 10^9\,M_\odot$, and separately stack the HI 21 cm cubes of the galaxies in each subsample. The stacked HI 21 cm emission signal is indeed detected separately in the two stellar mass subsamples, albeit at lower statistical significance, at $\approx$(3.4–3.7)σ level. We obtain average HI masses of $\langle M_{HI} \rangle = (2.95 \pm 0.87) \times 10^{10}\,M_\odot$ and $\langle M_{HI} \rangle = (3.23 \pm 0.88) \times 10^{10}\,M_\odot$ for the lower stellar mass ($\langle M_* \rangle = 4.0 \times 10^9\,M_\odot$) and higher stellar mass ($\langle M_* \rangle = 2.0 \times 10^{10}\,M_\odot$) subsamples, respectively.

Finally, we note that the DEEP2 survey is complete for galaxies with rest-frame B-band magnitude $M_B \leqslant -21$ (Willmer et al. 2006; Newman et al. 2013). We hence stacked the HI 21 cm spectra of the 2254 galaxies of our sample with $M_B \leqslant -21$, following the above procedure. This too yielded a clear detection (with $\approx 4.4\sigma$ significance) of the average HI 21 cm signal, but from a complete sample of galaxies. Integrating over the detected HI 21 cm line profile, we find that blue star-forming galaxies with $M_B \leqslant -21$ at $z \approx 1.3$ have an average HI mass of $\langle M_{HI} \rangle = (3.04 \pm 0.69) \times 10^{10}\,M_\odot$; this average HI mass is consistent with that obtained for the full sample of galaxies.

4. Stacking the Rest-frame 1.4 GHz Continuum Emission: The Radio SFR

The rest-frame 1.4 GHz luminosity ($L_{1.4\ GHz}$) of a galaxy can be used to determine its total SFR, via the far-infrared–radio correlation (e.g., Yun et al. 2001; Pannella et al. 2015; Bera et al. 2018). We initially convolved all our 610 MHz continuum images of the DEEP2 subfields (see Figure 1) to a common beam of size $6\farcs1 \times 6\farcs1$. For subfields 31/32 and 32/33 of Kanekar et al. (2016), we used the images of Bera et al. (2018), also convolved to the same beam; however, for subfields 21 and 22, we use the new, deeper images of Figure 1. From the convolved images, we extract cutouts of size $25'' \times 25''$ around each of our 2832 galaxies. We also extract identically sized cutouts $100''$ away from each galaxy, to test for the presence of systematic effects. For each galaxy, we convert the flux density S_ν at each pixel of its subimage to the corresponding rest-frame 1.4 GHz luminosity, assuming a typical spectral index of $\alpha = -0.8$, with $S_\nu \propto \nu^\alpha$ (Condon 1992). For the galaxies of our sample, the observing frequencies are very close to rest-frame 1.4 GHz; our results are hence insensitive to the exact choice of spectral index.

We used a median-stacking approach (e.g., White et al. 2007) to estimate the average $L_{1.4\ GHz}$ of the sample. This was done by computing the weighted median of each pixel across the sample, with the weights being the same as used while stacking their HI 21 cm emission. Figure 4(A) shows the average $L_{1.4\ GHz}$ emission from the 2841 galaxies; the image shows a clear detection of the stacked continuum emission, at $\approx 12\sigma$ statistical significance. No evidence for systematic effects is discernible in the offset-stack image of Figure 4(B). We obtain a median rest-frame 1.4 GHz luminosity of $L_{1.4\ GHz} = (3.93 \pm 0.30) \times 10^{22}$ W Hz^{-1}. Using the SFR calibration of Yun et al. (2001), this implies[7] a median SFR of $(14.5 \pm 1.1)\,M_\odot$ yr^{-1} for the 2841 galaxies of our sample.

5. Discussion

Our detection of the stacked HI 21 cm emission signal of Figure 2 is only the second, after Chowdhury et al. (2020), of HI 21 cm emission at $z \gtrsim 1$! The observations reported here used receivers, signal path, and correlator that were different from the system used by Chowdhury et al. (2020), and, of course, were affected differently by any time-variable RFI. The present detection of the HI 21 cm emission signal, and the measurement of the average HI mass of star-forming galaxies at $z \approx 1.3$, are hence important independent confirmations of the results of Chowdhury et al. (2020).

Our sample of 2841 blue star-forming galaxies at $z \approx 1.3$ has a mean stellar mass of $\langle M_* \rangle = 1.2 \times 10^{10}\,M_\odot$. Our radio-derived average SFR estimate of $(14.5 \pm 1.1) M_\odot$ yr^{-1} then implies that the average properties of our galaxies are consistent with those of the star-forming main sequence at $z \approx 1.3$ (e.g., Whitaker et al. 2012; Leslie et al. 2020).

Our measurement of a mean HI mass of $\langle M_{HI} \rangle = (3.09 \pm 0.61) \times 10^{10}\,M_\odot$ implies that the typical HI masses of main-sequence galaxies at $z \approx 1.3$ are significantly larger than their stellar masses, with an average HI-to-stellar mass ratio of 2.6 ± 0.5. This is very different from the situation in the local universe, where the HI-to-stellar mass ratio is only ≈ 0.4, for blue star-forming galaxies with a similar stellar mass distribution in the xGASS sample (e.g., Saintonge et al. 2017; Chowdhury et al. 2020).[8]

[6] The individual stellar masses of the galaxies were inferred from a relation between the $(U - B)$ color and the ratio of the stellar mass to the B-band luminosity, calibrated at $z \approx 1$ using stellar masses estimated from K-band observations of a subset of the DEEP2 sample (Weiner et al. 2009).

[7] All stellar masses and SFRs assume a Chabrier initial mass function.

[8] We estimate the average HI mass to average stellar mass ratio of the xGASS sample by taking a ratio of the weighted-mean HI mass and the weighted-mean stellar mass of star-forming galaxies, with NUV-$r < 4$, in the xGASS sample; the weights for each xGASS galaxy were chosen such that their effective stellar mass distribution is identical to that of our 2841 galaxies at $z \approx 1.3$. We note that xGASS contains galaxies with $M_* > 10^9\,M_\odot$ while our sample goes down to $M_* \approx 10^8\,M_\odot$, but this has a negligible effect on the comparison since only $\approx$2% of our sample of 2841 galaxies at $z \approx 1.3$ have $M_* < 10^9\,M_\odot$.

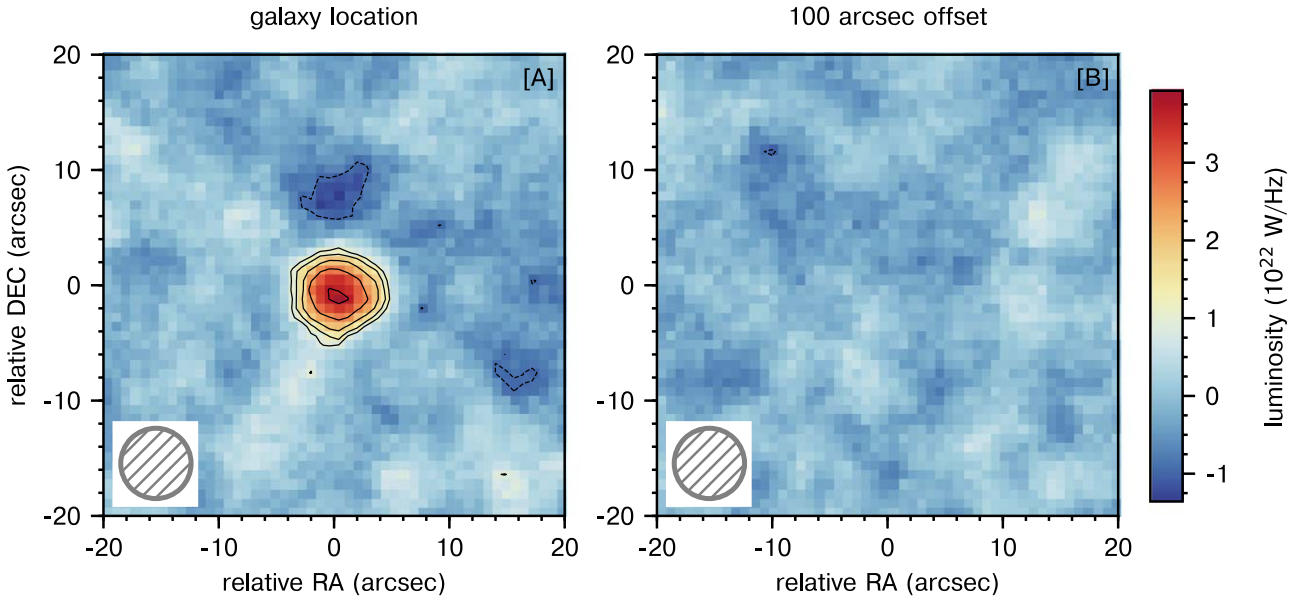

Figure 4. (A) The average rest-frame 1.4 GHz luminosity of our 2841 star-forming galaxies, obtained from a weighted-median stack of their rest-frame 1.4 GHz emission. A clear ($\approx 12\sigma$ significance) detection of the median 1.4 GHz emission of the galaxies can be seen in the image. (B) The result of the offset stack, a weighted-median stack at locations 100″ offset from the above galaxies: no signal is seen in this image. The circle at the bottom left of each panel shows the 6.″1 resolution of the images. The contours are at $(-3.0, 3.0, 4.2, 6.0, 8.4, 12.0) \times \sigma$, with dashed negative contours.

We measure an average HI mass of $\langle M_{HI} \rangle = (2.95 \pm 0.87) \times 10^{10}\,M_\odot$ and $\langle M_{HI} \rangle = (3.23 \pm 0.88) \times 10^{10}\,M_\odot$ in the two stellar mass subsamples, with average stellar masses of $4 \times 10^9\,M_\odot$ and $2 \times 10^{10}\,M_\odot$, respectively. This implies average HI mass to stellar mass ratios of 7.4 ± 2.2 and 1.60 ± 0.44, in the lower and higher stellar mass samples, respectively, again for blue star-forming galaxies at $z \approx 1.3$. While this tentatively suggests (at $\approx 2.6\sigma$ significance) that galaxies with low stellar masses are more gas-rich than those with high stellar masses (as has been seen in the local universe; e.g., Catinella et al. 2018), our current signal-to-noise ratio is not sufficient to determine the dependence of the HI-to-stellar mass ratio on the stellar mass.

CO emission studies of similar main-sequence galaxies at $z \approx 1$–2 have shown that their molecular gas mass is comparable to the stellar mass (e.g Tacconi et al. 2020). Our results thus indicate that the atomic gas content of star-forming galaxies at this epoch is larger than their molecular gas content. Further, at this epoch, star-forming galaxies contain nearly four times more cold gas, including both atomic and molecular gas, than stars, very different from the local universe.

The HI depletion timescale, $t_{dep,HI} \equiv M_{HI}/SFR$, provides an estimate of how long a galaxy's HI can fuel its star formation (with an intermediate conversion to H_2) at its current SFR. Combining our estimates of the average SFR and the average HI mass yields an average HI depletion timescale of $\langle t_{dep,HI} \rangle = 2.13 \pm 0.45$ Gyr for star-forming galaxies at $z \approx 1.3$. This is similar to the HI depletion timescale of 1–2 Gyr obtained by Chowdhury et al. (2020), for star-forming galaxies at $z \approx 1.0$. In the local universe, the HI depletion time in main-sequence galaxies with a stellar mass distribution similar to that of our sample is ≈ 7 Gyr (e.g., Saintonge et al. 2017). Our results (and those of Chowdhury et al. 2020) thus indicate that the HI depletion time changes significantly from $z \approx 1.3$ to $z = 0$, by a factor of $\gtrsim 3.5$.

In local galaxies, the H_2 depletion timescale, t_{dep,H_2}, is relatively short, $\lesssim 1$ Gyr (e.g., Tacconi et al. 2020), far smaller than the HI depletion timescale ($\approx$5–10 Gyr, depending on the stellar mass; e.g., Saintonge et al. 2017). Hence, star formation activity in local galaxies is not typically limited by the HI depletion timescale, as there is sufficient time for the HI to be replenished, via either accretion from the circumgalactic medium (CGM) or mergers. As such, main-sequence galaxies in the local universe can continue to quiescently form stars at their current SFR for $\approx$5–10 Gyr without the need for fresh gas accretion, as long as there is efficient conversion of HI to H_2 (on timescales shorter than t_{dep,H_2}). Conversely, main-sequence galaxies at $z \approx 1.3$ can sustain their current SFR for only ≈ 2 Gyr, unless their HI reservoir is replenished. The short HI depletion timescale could thus be a bottleneck for continued star formation activity, in the absence of the acquisition of new HI from CGM accretion or mergers. We note that the HI depletion time of ≈ 2 Gyr is comparable to the timescale on which the cosmic SFR density is observed to begin its steep decline. Our results are thus consistent with the hypothesis of Bera et al. (2018) and Chowdhury et al. (2020) that the quenching of star formation activity at $z < 1$ may arise due to insufficient gas accretion, resulting in a paucity of neutral gas to fuel further star formation.

In passing, we note that Chowdhury et al. (2020) obtained an average HI mass of $\langle M_{HI} \rangle = (1.19 \pm 0.26) \times 10^{10}\,M_\odot$ for 7653 star-forming galaxies at $z = 0.74$–1.45, also in the DEEP2 fields. While this average HI mass appears to be lower than our estimate, the wider redshift coverage of Chowdhury et al. (2020) implies that the stellar mass and luminosity distributions of the two samples are not the same. For example, the average absolute B-band magnitude of the 7653 galaxies of Chowdhury et al. (2020) is $\langle M_B \rangle = -20.9$, while that of the 2841 galaxies in our sample is $\langle M_B \rangle = -21.4$, i.e., the former sample contains more faint galaxies than our sample. We hence restricted the comparison to galaxies with $M_B \leqslant -21$, the completeness limit of the DEEP2 survey (Newman et al. 2013). The 3499 such galaxies of Chowdhury et al. (2020) yield $\langle M_{HI} \rangle = (1.70 \pm 0.43) \times 10^{10}\,M_\odot$ at $\langle z \rangle \approx 1.0$, while we obtain

$\langle M_{HI} \rangle = (3.04 \pm 0.69) \times 10^{10}\, M_{\odot}$ at $\langle z \rangle \approx 1.3$, consistent at $\approx 1.6\sigma$ significance. We thus find no evidence for redshift evolution in the average HI mass from $z \approx 1.3$ to $z \approx 1.0$.

6. Summary

We report a ≈400 hr GMRT HI 21 cm emission survey of the DEEP2 fields, carried out using the original GMRT 610 MHz receivers and the legacy narrowband GMRT correlator, which (including 60 hr of earlier data with the same system) has yielded only the second detection of redshifted HI 21 cm emission from galaxies at $z \gtrsim 1$. We stacked the HI 21 cm emission from 2841 blue star-forming, main-sequence galaxies at $z = 1.18$–1.39 to obtain a 5.0σ significance detection of the average HI 21 cm emission signal of the galaxies. This implies an average HI mass of $\langle M_{HI} \rangle = (3.09 \pm 0.61) \times 10^{10}\, M_{\odot}$ for blue star-forming galaxies at $\langle z \rangle = 1.3$. We obtain an HI-to-stellar mass ratio of 2.6 ± 0.5, significantly higher than that of similar galaxies in the local universe. We use our radio-continuum images to infer an average SFR of $(14.5 \pm 1.1)\, M_{\odot}$/yr for the same 2841 galaxies and combine this with our average HI mass estimate to obtain an average HI depletion timescale of (2.13 ± 0.45)Gyr, consistent with the results of Chowdhury et al. (2020), and far shorter than the HI depletion timescale of galaxies with similar stellar masses in the local universe. The short HI depletion timescale is comparable to the timescale on which the cosmic SFR density declines after its peak at $z \approx 1 - 3$. Our results are thus consistent with the hypothesis that the availability of HI in galaxies at $z \approx 1$ may been a critical bottleneck in quenching their star formation, which led to the observed decline in the cosmic SFR density at $z < 1$.

We thank the staff of the GMRT who have made these observations possible. The GMRT is run by the National Centre for Radio Astrophysics of the Tata Institute of Fundamental Research. N.K. acknowledges support from the Department of Science and Technology via a Swarnajayanti Fellowship (DST/SJF/PSA-01/2012-13). A.C., N.K., and B.D. also acknowledge the Department of Atomic Energy for funding support, under project 12-R&D-TFR-5.02-0700.

Software: CASA (McMullin et al. 2007), calR (Chowdhury 2021), AOFLAGGER (Offringa et al. 2012), astropy (Astropy Collaboration et al. 2013, 2018).

ORCID iDs

Aditya Chowdhury https://orcid.org/0000-0002-5795-517X
Nissim Kanekar https://orcid.org/0000-0002-9757-7206
Barnali Das https://orcid.org/0000-0001-8704-1822

References

Astropy Collaboration, Price-Whelan, A. M., Sipőcz, B. M., et al. 2018, AJ, 156, 123
Astropy Collaboration, Robitaille, T. P., Tollerud, E. J., et al. 2013, A&A, 558, A33
Bera, A., Kanekar, N., Chengalur, J. N., & Bagla, J. S. 2019, ApJL, 882, L7
Bera, A., Kanekar, N., Weiner, B. J., Sethi, S., & Dwarakanath, K. S. 2018, ApJ, 865, 39
Bouwens, R. J., Illingworth, G. D., Oesch, P. A., et al. 2010, ApJL, 709, L133
Briggs, D. S. 1995, AAS Meeting, 187, 112.02
Catinella, B., Saintonge, A., Janowiecki, S., et al. 2018, MNRAS, 476, 875
Chengalur, J. N., Braun, R., & Wieringa, M. 2001, A&A, 372, 768
Chowdhury, A. 2021, calR: Robust Calibration in CASA, v3.3.1, Zenodo, doi:10.5281/zenodo.4723688
Chowdhury, A., Kanekar, N., Chengalur, J. N., Sethi, S., & Dwarakanath, K. S. 2020, Natur, 586, 369
Condon, J. J. 1992, ARA&A, 30, 575
Condon, J. J., Cotton, W. D., & Broderick, J. J. 2002, AJ, 124, 675
Cornwell, T. J., Golap, K., & Bhatnagar, S. 2008, ISTSP, 2, 647
Fernández, X., Gim, H. B., van Gorkom, J. H., et al. 2016, ApJL, 824, L1
Hopkins, A. M., & Beacom, J. F. 2006, ApJ, 651, 142
Kanekar, N., Sethi, S., & Dwarakanath, K. S. 2016, ApJL, 818, L28
Lah, P., Chengalur, J. N., Briggs, F. H., et al. 2007, MNRAS, 376, 1357
Le Floc'h, E., Papovich, C., Dole, H., et al. 2005, ApJ, 632, 169
Leslie, S. K., Schinnerer, E., Liu, D., et al. 2020, ApJ, 899, 58
Madau, P., & Dickinson, M. 2014, ARA&A, 52, 415
Maddox, N., Hess, K. M., Blyth, S. L., & Jarvis, M. J. 2013, MNRAS, 433, 2613
McMullin, J. P., Waters, B., Schiebel, D., Young, W., & Golap, K. 2007, in ASP Conf. Ser. 376, CASA Architecture and Applications, ed. R. A. Shaw, F. Hill, & D. J. Bell (San Francisco, CA: ASP), 127
Newman, J. A., Cooper, M. C., Davis, M., et al. 2013, ApJS, 208, 5
Offringa, A. R., van de Gronde, J. J., & Roerdink, J. B. T. M. 2012, A&A, 539, A95
Pannella, M., Elbaz, D., Daddi, E., et al. 2015, ApJ, 807, 141
Rau, U., & Cornwell, T. J. 2011, A&A, 532, A71
Rhee, J., Lah, P., Chengalur, J. N., Briggs, F. H., & Colless, M. 2016, MNRAS, 460, 2675
Saintonge, A., Catinella, B., Tacconi, L. J., et al. 2017, ApJS, 233, 22
Tacconi, L. J., Genzel, R., & Sternberg, A. 2020, ARA&A, 58, 157
Weiner, B. J., Coil, A. L., Prochaska, J. X., et al. 2009, ApJ, 692, 187
Whitaker, K. E., van Dokkum, P. G., Brammer, G., & Franx, M. 2012, ApJL, 754, L29
White, R. L., Helfand, D. J., Becker, R. H., Glikman, E., & de Vries, W. 2007, ApJ, 654, 99
Willmer, C. N. A., Faber, S. M., Koo, D. C., et al. 2006, ApJ, 647, 853
Yun, M. S., Reddy, N. A., & Condon, J. J. 2001, ApJ, 554, 803
Zwaan, M. A. 2000, PhD Thesis, Rijksuniversiteit Groningen